

# Crystal structure of a bacterial homologue of glucose transporters GLUT1–4

Linfeng Sun<sup>1,2,3\*</sup>, Xin Zeng<sup>1,2,3\*</sup>, Chuangye Yan<sup>1,2,3</sup>, Xiuyun Sun<sup>2</sup>, Xinqi Gong<sup>1,2,3</sup>, Yu Rao<sup>2</sup> & Nieng Yan<sup>1,2,3</sup>

Glucose transporters are essential for metabolism of glucose in cells of diverse organisms from microbes to humans, exemplified by the disease-related human proteins GLUT1, 2, 3 and 4. Despite rigorous efforts, the structural information for GLUT1–4 or their homologues remains largely unknown. Here we report three related crystal structures of XylE, an *Escherichia coli* homologue of GLUT1–4, in complex with D-xylose, D-glucose and 6-bromo-6-deoxy-D-glucose, at resolutions of 2.8, 2.9 and 2.6 Å, respectively. The structure consists of a typical major facilitator superfamily fold of 12 transmembrane segments and a unique intracellular four-helix domain. XylE was captured in an outward-facing, partly occluded conformation. Most of the important amino acids responsible for recognition of D-xylose or D-glucose are invariant in GLUT1–4, suggesting functional and mechanistic conservations. Structure-based modelling of GLUT1–4 allows mapping and interpretation of disease-related mutations. The structural and biochemical information reported here constitutes an important framework for mechanistic understanding of glucose transporters and sugar porters in general.

Glucose is an essential fuel for most living organisms on Earth. Uptake of glucose into mammalian cells is mediated mainly by members of the GLUT (or SLC2A for solute carrier 2A) and SGLT families of transporters<sup>1–3</sup>. GLUTs, which are major facilitator superfamily (MFS)-type passive transporters, catalyse the facilitative diffusion of glucose and other hexoses across the plasma membrane. By contrast, SGLTs are LeuT-type, Na<sup>+</sup>-dependent secondary active symporters<sup>4</sup>.

Among the 14 human GLUT family members, GLUT1–4 have been rigorously investigated because of their fundamental roles in a multitude of physiological and pathophysiological processes<sup>2,5</sup>. GLUT1, the first glucose transporter cloned<sup>6</sup>, is responsible for glucose uptake into erythrocytes and the transport across blood–brain barrier. Mutations of GLUT1 may lead to GLUT1 deficiency syndrome (also known as De Vivo disease), manifested by a broad spectrum of clinical phenotypes including infantile-onset seizure<sup>7–9</sup>. GLUT2 is highly expressed in pancreatic  $\beta$ -cell, intestine, kidney and liver, and is associated with the Fanconi–Bickel syndrome<sup>10,11</sup>. GLUT3 is the main neuronal glucose transporter<sup>12</sup>. The expression levels of GLUT1 and GLUT3 are enhanced in some carcinoma cell lines for increased glucose supply in cancer cells (the Warburg effect)<sup>12–14</sup>. GLUT4 is the main glucose transporter in muscles and adipocytes. Unlike other GLUTs, the cellular localization of GLUT4 is regulated by insulin through a complex mechanism whose aberration contributes to obesity and type 2 diabetes mellitus<sup>15–17</sup>.

GLUT1–4 belong to the sugar porter (SP) family (TCDB transporter classification 2.A.1.1)<sup>18</sup>, which represents a large and ubiquitous MFS subfamily consisting of members derived from bacteria, archaea, cyanobacteria, fungi, protozoa, plants and animals (Supplementary Figs 1 and 2)<sup>19</sup>. SP subfamily proteins, such as the hexose transporters in yeasts<sup>20</sup> and the sucrose transporters in plants<sup>21,22</sup>, have been subject to extensive characterizations for their essential roles in hexose and disaccharide metabolism. GLUT transporters and their homologues have been the targets of rigorous, albeit unsuccessful, structural investigations. Sequence analysis and biochemical characterizations have helped in deducing the boundaries of the transmembrane segments (TMs) for

GLUTs<sup>6,23</sup>. The structures of several MFS members have been reported<sup>24–28</sup>. Nevertheless, the lack of sequence similarity between these MFS proteins and GLUT family members has made it a daunting task to generate accurate structure-based models of GLUT1–4.

To elucidate the structure and molecular mechanism of GLUT1–4, we launched a systematic effort to screen for well-behaved GLUT1–4 protein variants as well as their homologues. Among the tested proteins, the *E. coli* D-xylose:H<sup>+</sup> symporter XylE<sup>29–33</sup> showed excellent solution behaviour. XylE, an archetypal member of the SP subfamily<sup>19,32</sup>, shares sequence identities of 29%, 30%, 29% and 27%, and similarities of 49%, 51%, 48% and 47%, with GLUT1, GLUT2, GLUT3 and GLUT4, respectively (Supplementary Fig. 1). Here we report the crystal structures of XylE bound separately to three different ligands: D-xylose, D-glucose and 6-bromo-6-deoxy-D-glucose (6-BrGlc). We also performed an extensive, structure-guided, *in vivo* and *in vitro* functional analysis of XylE. These studies reveal significant insights into the structure and function of XylE and its human homologues GLUT1–4.

## Structure of D-xylose-bound XylE

The purified, recombinant XylE binds to D-xylose with a dissociation constant ( $K_d$ ) of about  $0.35 \pm 0.03$  mM (mean  $\pm$  s.d.) as measured by isothermal titration calorimetry, and transports D-xylose in a pH-dependent manner with a  $K_m$  of  $0.47 \pm 0.05$  mM at pH 6.5 as measured by proteoliposome-based counterflow assay (Supplementary Fig. 3). The addition of ligand proved essential for the successful generation of well-diffracting XylE crystals. The structure of XylE bound to D-xylose was determined and refined to 2.8 Å resolution (Fig. 1, Supplementary Fig. 4 and Supplementary Table 1).

XylE contains a typical MFS fold of 12 TMs, with amino and carboxy termini both located on the intracellular side (Fig. 1). The 12 TMs are organized into two distinct domains—the N and C domains—which can be superimposed with a root mean square deviation of 3.11 Å over 153 C $\alpha$  atoms (Supplementary Fig. 5a). TM7 and TM10 are both discontinuous helices (Supplementary Fig. 5b), which may facilitate conformational changes during substrate transport<sup>34</sup>.

<sup>1</sup>State Key Laboratory of Bio-membrane and Membrane Biotechnology, Center for Structural Biology, Tsinghua University, Beijing 100084, China. <sup>2</sup>School of Life Sciences and School of Medicine, Tsinghua University, Beijing 100084, China. <sup>3</sup>Tsinghua-Peking Center for Life Sciences, Tsinghua University, Beijing 100084, China.

\*These authors contributed equally to this work.

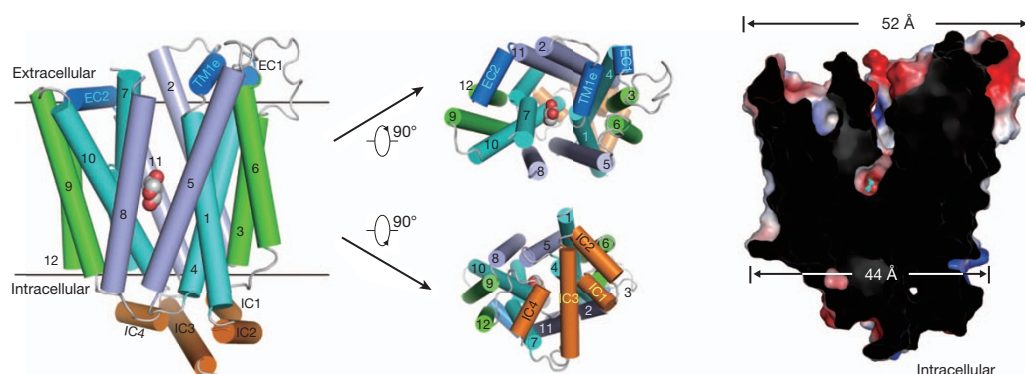


**Figure 1 | The structure of XylE bound to D-xylose has an outward-facing, partly occluded conformation.** Left: the overall structure of XylE bound to D-xylose. Three perpendicular views are shown. The corresponding TM segments in the four 3-helix bundles, which constitute the typical MFS structural fold, are coloured the same. D-Xylose is shown in space-filling model. The extracellular and intracellular helices are coloured sea-blue and orange,

respectively. Right: D-xylose resides in the centre of the structure, occluded from intracellular side and solvent-accessible from the extracellular side. A cut-open view of the surface electrostatic potential is shown here. The surface electrostatic potential was calculated with PyMol<sup>50</sup>. All structure figures were prepared with PyMol.

The overall structure of XylE has an outward-facing conformation. The ligand D-xylose is trapped within the centre of the transmembrane domain, completely occluded from the intracellular side yet solvent-accessible from the extracellular side through a channel, which is too narrow to allow the escape of D-xylose (Fig. 1 and Supplementary Fig. 5c). The structure of XylE was therefore captured in a ligand-bound, outward-facing, partly occluded conformation, which may represent an important expansion to the collection of MFS conformations.

Unlike other MFS transporters of known structure<sup>35</sup>, XylE contains an intracellular domain that comprises four helices, three connecting the N and C domains, and one at the C-terminal end (Fig. 1 and Supplementary Fig. 1b). The intracellular helices interact with the cytosolic portion of the TMs through extensive polar interactions (Supplementary Fig. 6). The residues that constitute the intracellular helices are highly conserved in GLUT1–4. In particular, most of the residues that mediate the inter-domain interactions are invariant in XylE and GLUT1–4 (Supplementary Figs 1b and 6). On the basis of this analysis, we predict that a similar cytoplasmic domain is likely to exist in GLUT1–4 and may interact with the TMs of GLUT1–4, as observed in XylE.

### Coordination of D-xylose

One molecule of D-xylose is bound between the N and C domains, closer to the latter (Supplementary Fig. 7a). D-Xylose is coordinated by both polar and aromatic residues mainly from the C domain (Fig. 2a, b). Unlike other proton symporters<sup>24,27,36</sup>, no charged residue is observed in ligand binding in XylE. The hydroxyl groups of D-xylose are specifically recognized, through a total of eight hydrogen bonds, by polar residues including Gln 168 on TM5, Gln 288/Gln 289/Asn 294 on TM7, Trp 392 on TM10, and Gln 415 on TM11 (Fig. 2b and Supplementary Fig. 7b). Tyr 298 and Gln 415 also contribute to substrate binding through water-mediated hydrogen bonds (Supplementary Fig. 7c).

Several aromatic residues, including Phe 24 on TM1, Tyr 298 on TM7, Trp 392 on TM10, and Trp 416 on TM11, are located in the vicinity of D-xylose (Fig. 2b). The presence of aromatic residues surrounding the substrate is commonly observed in membrane transporters<sup>4,36–40</sup>. Among these aromatic residues, Tyr 298 constitutes the constriction that may prevent the escape of D-xylose to the extracellular side (Figs 1 and 2a, b). Except for Phe 24 and Gln 168, all other ligand-binding residues are from the C domain. In particular, the kinked TM7 is important in substrate coordination by contributing three polar residues, namely Gln 288, Gln 289 and Asn 294, and one aromatic residue, Tyr 298 (Fig. 2b).

To examine the role of these residues in D-xylose transport, we generated several XylE variants, each containing replacement of a specific ligand-binding residue by Ala (Fig. 2c), and examined their transport activities using both a cell-based uptake assay and a proteoliposome-based counterflow experiment. Missense mutation of any of the eight amino acids Gln 168, Gln 288, Gln 289, Asn 294, Tyr 298, Trp 392, Gln 415 and Trp 416 led to nearly complete abrogation of the transport activity in both assays. Mutation of Phe 24 also resulted in significant impairment of the transport activity. By contrast, mutation of Asn 325,

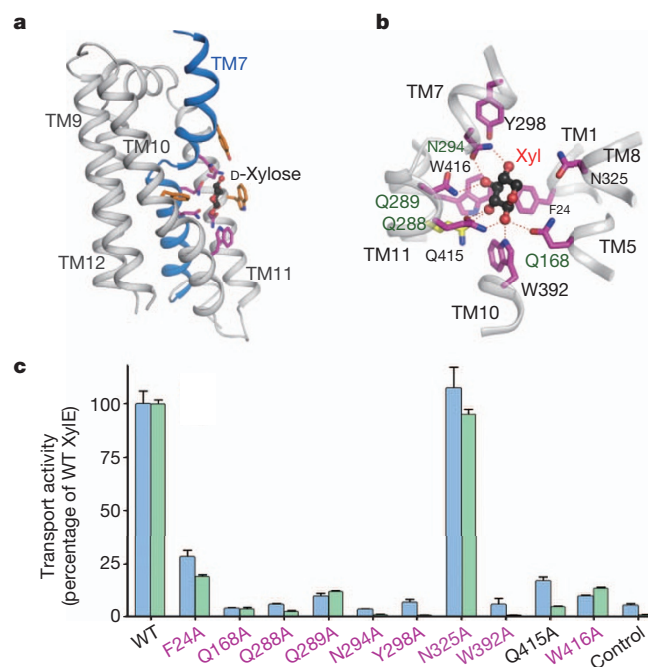


**Figure 2 | Recognition of D-xylose by XylE.** **a**, D-Xylose is coordinated mainly by residues from the C domain. The surrounding polar and aromatic residues are shown in magenta and orange sticks, respectively. D-Xylose is shown in black ball-and-sticks. **b**, D-Xylose is coordinated by both polar and aromatic residues. The residues that are invariant in XylE and GLUT1–4 are coloured magenta. **c**, Examination of the role of the ligand-binding residues in the transport of D-xylose in both cell-based uptake (blue bars) and proteoliposome-based counterflow (green bars) assays. Mutations of the invariant residues are labelled in magenta. The transport activities of XylE variants are normalized against those of the WT protein. Control refers to the uptake by *xylE*-deficient *E. coli* cells transformed with empty vector in the whole-cell assay, or liposome without protein in the counterflow assay. Error bars represent s.d.

which is not directly involved in ligand binding, showed slightly increased activity in the cell-based uptake and retained nearly full activity in the counterflow assay. The biochemical analysis is fully consistent with the structural observations.

### Specificity of substrate recognition by XylE

D-Xylose is specifically recognized by residues in XylE through hydrogen bonds. Except for Gln 415, all other residues involved in D-xylose recognition are completely invariant in GLUT1–4 (Supplementary Fig. 1b). This analysis suggests that D-glucose, and perhaps other pentoses and hexoses, might be recognized by XylE. We investigated the ability of six distinct sugar molecules to compete with D-xylose for transport by XylE in counterflow experiments (Fig. 3a and Supplementary Fig. 8a). Although five of the sugars had little effect on the transport of D-xylose, D-glucose showed pronounced inhibition, decreasing the transport activity by nearly 90% (Fig. 4a), confirming with the purified protein the specificity originally deduced for XylE from *in vivo* measurements of xylose:H<sup>+</sup> symport<sup>19</sup>.

The observed inhibition by D-glucose can be rationalized by the similarity between the chemical structures of D-xylose and D-glucose, the latter having only one extra 6-hydroxymethyl group (Supplementary Fig. 8a). Furthermore, isothermal titration calorimetry experiments revealed that D-glucose binds to XylE with a  $K_d$  of about  $0.77 \pm 0.01$  mM (Supplementary Fig. 8b), similar to that between D-xylose and XylE (Supplementary Fig. 3a). Consistent with *in vivo* observations<sup>19</sup>, D-glucose is not a transport substrate for XylE (Fig. 3a, inset), suggesting additional structural elements for the transport activity of XylE towards D-xylose but not towards D-glucose. These results further indicate that, under physiological conditions, abundant D-glucose may serve as an inhibitor of the D-xylose transporter—perhaps as a method of preserving resources<sup>19,41</sup>.

### Coordination of D-glucose by XylE

Next, we sought to determine the crystal structure of XylE bound to D-glucose. Following generally the same protocols as those for the XylE–D-xylose complex, we succeeded in crystallizing XylE in the presence of 40 mM D-glucose. The structure was refined to 2.9 Å resolution (Supplementary Table 1). The overall protein conformation remains identical to that of XylE bound to D-xylose. To precisely determine the location and orientation of D-glucose in the structure, we chemically synthesized a D-glucose derivative, 6-BrGlc, and crystallized XylE bound to it. The diffraction data were collected at the wavelength for Br anomalous signal and the structure was refined at 2.6 Å resolution with excellent quality (Supplementary Table 1). The position of the Br atom was unambiguously identified by the strong

anomalous signal, which not only allowed the determination of the orientation of D-glucose but also confirmed that of D-xylose (Supplementary Fig. 9).

As predicted by our biochemical analysis and sequence conservation, the coordination of D-glucose by XylE is very similar to that of D-xylose (Fig. 3b and Supplementary Fig. 10). In comparison with D-xylose coordination, Gln 168 seems to have a more prominent function in binding to D-glucose, in that it forms three hydrogen bonds with D-glucose. An extra hydrogen bond is found between the carbonyl oxygen of Gly 388 on TM10 and the 1-hydroxyl group of D-glucose. Gln 175, which is not involved in D-xylose binding, is hydrogen-bonded to the 6-hydroxyl group of D-glucose. The extra hydroxymethyl group of D-glucose is further coordinated through van der Waals contacts by Ile 171 on TM5 and Phe 383 on TM10.

Except for Gln 175 and Gln 415, all other residues that mediate D-glucose recognition are invariant in GLUT1–4. Thus the structural information on XylE provides a molecular framework for understanding the structures and mechanisms of substrate recognition by the physiologically important glucose transporters (Fig. 3b and Supplementary Fig. 1b).

### XylE-based structural model of GLUT1

The high degree of sequence conservation between XylE and GLUT1–4, particularly involving the functionally important residues (Supplementary Fig. 1), allowed us to build detailed structural models for GLUT1–4 with the program JACKAL<sup>42</sup>. In these models, the invariant and conserved amino acids in GLUT1–4 are aligned with those in XylE, which underlies functional conservation. We believe that these homology-based models of GLUT1–4 more faithfully represent reality than those derived from sequence analysis or non-homologous LacY-based models.

The XylE-derived homology model of GLUT1 (Fig. 4a, b) reveals several significant findings. First, the new GLUT1 model contains a more accurate demarcation of the secondary structural elements. For example, the TM boundaries in previous models of GLUT1 in textbooks, represented by that on page 392 in the fifth edition of *Lehninger Principles of Biochemistry*, deviate considerably from our model. Second, similarly to XylE, the new GLUT1 model contains four  $\alpha$ -helices on the intracellular side (Fig. 4a, b) that were absent from previous models. Amino acids in this intracellular domain and their interacting residues in the TMs are highly conserved between XylE and GLUT1–4 (Supplementary Figs 1b and 6). Third, and most importantly, D-glucose recognition by GLUT1, as well as by GLUT2–4, should be nearly identical to that observed in the structure of D-glucose-bound XylE, because the vast majority of the amino acids involved in substrate

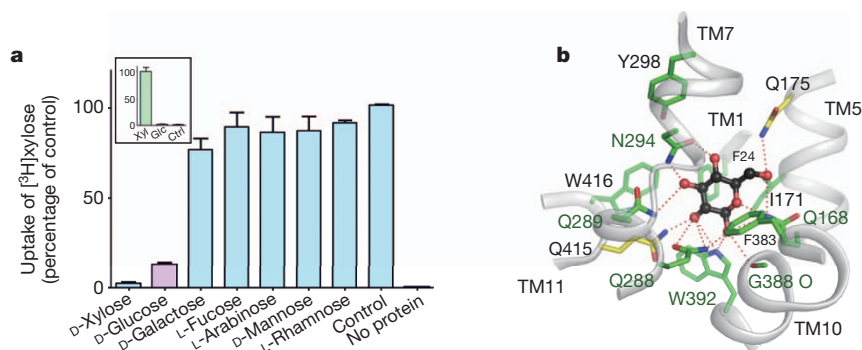


**Figure 3 | Coordination of D-glucose by XylE.** **a**, Substrate selectivity of XylE, as determined by liposome-based competition assay. Of the tested pentoses and hexoses, only D-glucose inhibited the transport of D-xylose by XylE, although D-glucose could not be transported by XylE (inset). Control, control experiment without the addition of sugar competitors; the averaged readout of the control experiments is set as 100%. Xyl, D-xylose; Glc, D-glucose; Ctrl, control experiment with XylE-free liposomes. **b**, Coordination of D-glucose by

XylE observed in the structure of XylE bound to D-glucose. D-Glucose is shown in black ball-and-sticks. Hydrogen bonds are represented by red dashed lines. The invariant residues in XylE and GLUT1–4 are coloured green. The position and orientation of D-glucose were verified by the bromide anomalous signal for a glucose derivative, 6-BrGlc, whose complex with XylE was determined at 2.6 Å resolution (Supplementary Fig. 9 and Supplementary Table 1).



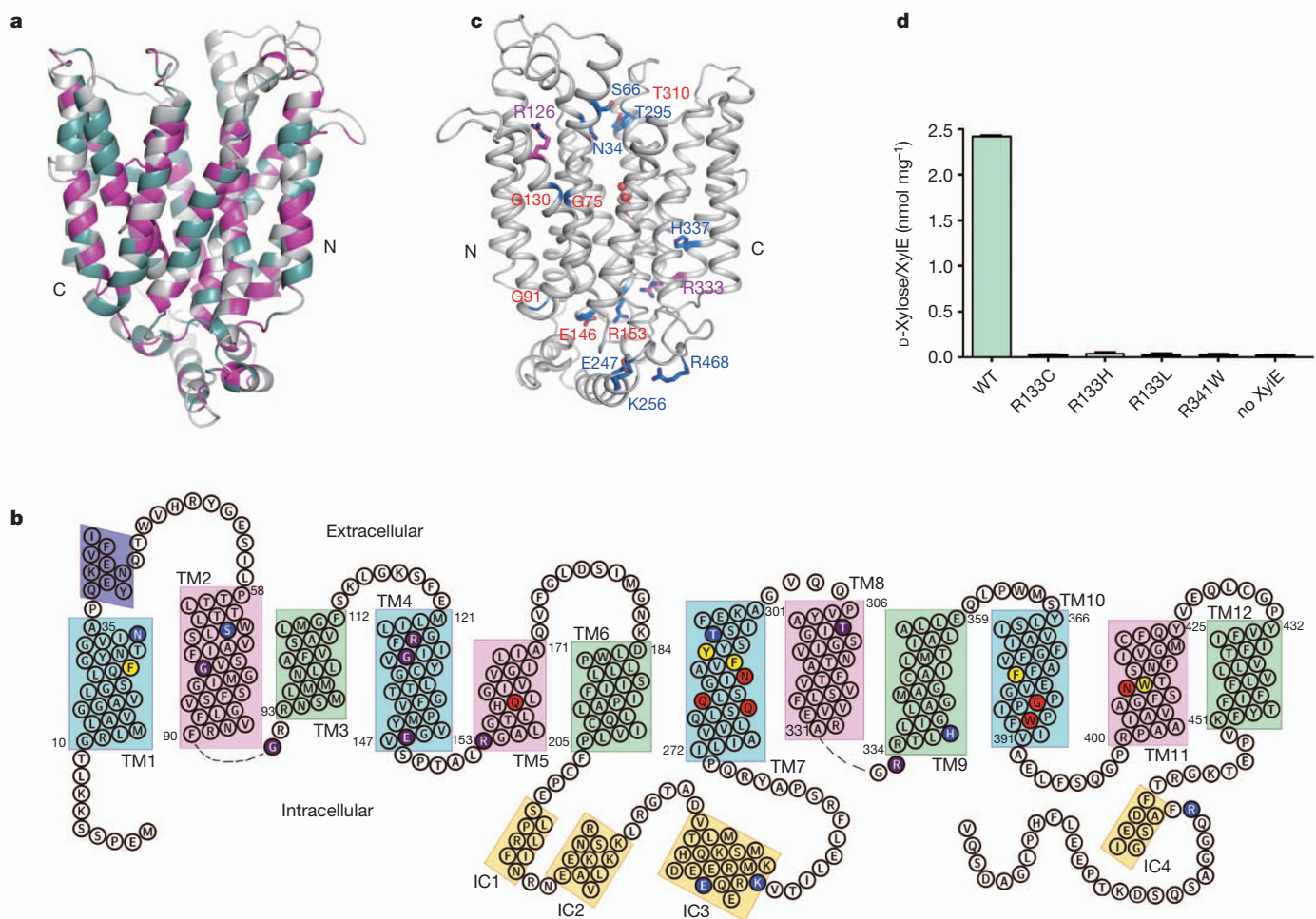


**Figure 4 | Homology-based modelling of GLUT1 structure.** **a**, A structural model of GLUT1 is generated on the basis of XylE structure and sequence conservation. Invariant and conserved residues are coloured magenta and dark green, respectively. **b**, Predicted secondary structural elements of GLUT1. Polar and aromatic residues predicted to be involved in D-glucose binding are shaded red and yellow, respectively. The residues whose mutations were found in GLUT1 deficiency syndrome are shaded purple and blue for invariant and

variant residues, respectively. **c**, Mapping of the disease-related residues on the structural model of GLUT1. Invariant and variant residues in XylE and GLUT1–4 are labelled red and blue, respectively. **d**, Mutation of Arg 133 or Arg 341 in XylE, which correspond to Arg 126 and Arg 333 of GLUT1 (highlighted in magenta in **c**), led to abrogation of D-xylose transport in a liposome-based counterflow assay.

binding are invariant between XylE and GLUT1–4 (Fig. 3b and Supplementary Figs 1b and 10).

We mapped disease-derived mutations onto the structural model of GLUT1 (Fig. 4c) and speculated on the potential impact of these mutations on GLUT1 transport activity<sup>43,44</sup>. None of these residues is directly involved in glucose binding as observed in the outward-facing, partly occluded conformation of XylE (Fig. 4b, c). Among the mutated residues, Asn 34, Ser 66, Thr 295 and Thr 310 are located on the extracellular side of the putative transport path, suggesting potential involvement in substrate transport. Gly 75 and Gly 130 are positioned in the middle of TM2 and TM4, respectively; their mutations probably lead to a steric clash or impairment of conformational flexibility required for transport activity. Arg 126 and His 337 are away from the transport path and buried within the N and C domains (Fig. 4c), implying a regulatory role for substrate transport. Intriguingly, several residues, including Gly 91, Glu 146, Arg 153, Glu 247, Lys 256, Arg 333 and Arg 468, are clustered on the intracellular side, with some contributing to the interactions between the intracellular  $\alpha$ -helices and the TMs (Fig. 4b, c and Supplementary Fig. 6). The fact that the interface involving the intracellular  $\alpha$ -helices is targeted for disease-causing mutations suggests functional significance of the intracellular domain.

Several of the disease-related residues in GLUT1 are invariant in XylE. We attempted to examine the effect of some of these mutations

on the transport activity of XylE. The XylE variants containing single missense mutations G67W (Gly 75 in GLUT1), G137S (Gly 130 in GLUT1) and R160L (Arg 153 in GLUT1) failed to yield well-behaved recombinant proteins, supporting a structural role for these residues. The variants containing Arg 133 (Arg 126 in GLUT1) mutations or R341W (R333W in GLUT1) gave rise to well-behaved recombinant proteins. These XylE variants, R133C, R133H, R133L and R341W, completely lost the transport activity for D-xylose (Fig. 4d), consistent with the observations that the corresponding mutations in GLUT1 led to a significant decrease in substrate transport, which are thought to be correlated with clinical disorders<sup>43,45,46</sup>.

### Functional significance of the SP signature motifs

The ligand-bound, outward-facing, partly occluded conformation of XylE is complementary to the other captured conformations for MFS proteins (Fig. 5a). The intramembrane helix domain of XylE is absent from the other MFS members of known structures. In particular, XylE has several distinct features in comparison with LacY and FucP, the other two MFS sugar:H<sup>+</sup> symporters.

XylE lacks charged residues in the vicinity of the substrate-binding site (Figs 2b and 3b), whereas Glu/Asp residues essential for both substrate binding and proton translocation were identified in both LacY<sup>47,48</sup> and FucP<sup>27</sup>. A large number of hydrogen-bond-forming

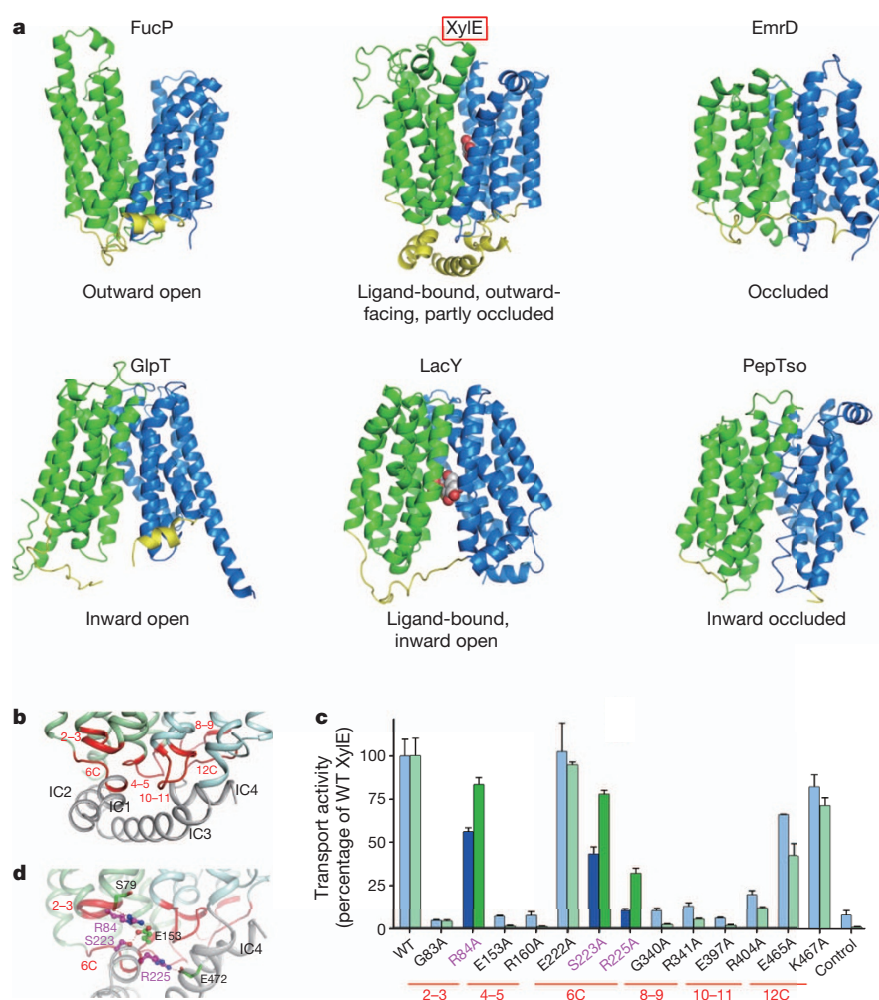


**Figure 5 | Functional significance of the conserved SP family signature motifs.**

**a**, Reported MFS structures display distinct conformations. XylE contains an intracellular helix domain (yellow) that is not seen in the other structures. The distinct N and C domains are coloured green and blue in all the structures. **b**, The SP family signature motifs (coloured red) are located on the intracellular side of XylE. The motifs are labelled according to their locations. For example, '2-3' refers to the one connecting TMs 2 and 3. The N domain is coloured pale green, and the C domain pale cyan. **c**, Functional characterization of the conserved motif residues. The motifs where the indicated residues are located are indicated at the bottom. The presentation scheme is identical to that of Fig. 2c. **d**, Structural analysis of the functionally characterized residues that may be involved in proton-coupled active transport.

residues are distributed on the interface between the TMs and the intracellular domain of XylE (Supplementary Fig. 6), but not in LacY or FucP. Furthermore, common to SP family members, but largely missing in LacY and FucP, conserved signature motifs are found in XylE<sup>19,32</sup>, including D(N)RXGRR between TMs 2 and 3 and TMs 8 and 9, E-----R between TMs 4 and 5 and TMs 10 and 11, and PESPR and PETK at the C termini of TM6 and TM12 (hereafter referred to as TM6C and TM12C motifs), respectively (Supplementary Figs 1 and 2). All of these motifs are positioned on the cytoplasmic side of the TMs except a couple of residues in the TM6C motif that are located in intracellular helix  $\alpha$ 1 (Fig. 5b and Supplementary Figs 1 and 2). Most of these motif residues are charged and polar ones that form an intricate hydrogen-bond network, mediating the interactions between the TMs and the intracellular domain (Supplementary Figs 1, 2 and 6).

To assess the functional importance of these motifs we generated a number of XylE variants each containing an Ala substitution of one conserved motif residue. Both cell-based uptake and proteoliposome-based counterflow experiments were performed for the variants that yielded reasonable protein expression and solution behaviours. More than half of the single point mutations resulted in completely abrogated or seriously impaired activities in both assays, indicating an essential role for the SP signature motifs for transport activity (Fig. 5c). A detailed analysis of the assay results can be found in Supplementary Discussion. Here we focus on three SP motif residues.

Mutation of Arg 84 or Ser 223 had a limited effect on the transport activity of XylE in the counterflow assay, but led to the loss of about half of the activity in the active uptake of D-xylose into the cell. Ala

replacement of Arg 225, which is located on intracellular helix  $\alpha$ 1, completely abolished the active transport but retained more than 30% of the activity in the counterflow assay. The distinct activities of these variants between cell uptake and counterflow experiments suggested that the three residues may be involved in active transport. This speculation seems to be supported by structural observations. Arg 84 and Ser 223 both form hydrogen bonds with Glu 153, whereas Arg 225 is hydrogen-bonded to Glu 472 (Fig. 5d). Protonation and deprotonation may affect hydrogen bond formation between these residues. Nonetheless, further interpretation is complicated by the fact that all three residues are invariant in the proton-gradient-independent uniporters GLUT1-4.

The biochemical characterizations reported here revealed that the SP motifs as well as the intracellular helix domain have a critical role for the function of XylE. Given that extensive hydrogen bonds are formed by these structural elements, some of the residues may contribute to proton symport. Nevertheless, it remains puzzling that all these residues are invariant in GLUT1-4 and XylE (Supplementary Fig. 1b), the former being facilitative uniporters and the latter being a proton symporter. The molecular determinants for the proton coupling in XylE remain to be established.

Here we have reported three related crystal structures of XylE, a bacterial homologue of the human proteins GLUT1-4, in complex with D-xylose, D-glucose and 6-BrGlc. The structural information, together with the biochemical inspections, provides a valuable framework for further deciphering the functional mechanisms of the physiologically important glucose transporters GLUT1-4 and other members of the SP family.



## METHODS SUMMARY

Full-length, wild-type (WT) XylE from *E. coli* strain O157:H7 was overexpressed in *E. coli* BL21(DE3) and purified to homogeneity in the presence of 0.2% (w/v) *n*-nonyl- $\beta$ -D-glucopyranoside and 0.02% (w/v) *n*-dodecyl-*N,N*-dimethylamine-*N*-oxide. The identity and structure of the synthesized 6-BrGlc were confirmed by both NMR and high-resolution mass spectrometry analysis. D-Xylose, D-glucose and 6-BrGlc were present at 20, 40 and 40 mM, respectively, for the crystallization of XylE bound to these ligands. Data sets were collected at Shanghai Synchrotron Radiation Facility beamline BL17U and SPring-8 beamline BL41XU. The initial phases were derived from mercury-based and platinum-based single-wavelength anomalous dispersion using the program ShelxC/D/E<sup>49</sup>. The binding affinity between the ligands and purified recombinant XylE was measured with isothermal titration calorimetry. The cell-based uptake assays and proteoliposome-based counterflow experiments were performed by following the published protocols<sup>27,36</sup>. The XylE-based homology model of human GLUT1 structure was generated with the software JACKAL<sup>42</sup>.

**Full Methods** and any associated references are available in the online version of the paper.

Received 12 March; accepted 17 August 2012.

- Thorens, B. & Mueckler, M. Glucose transporters in the 21st Century. *Am. J. Physiol. Endocrinol. Metab.* **298**, E141–E145 (2010).
- Pascual, J. M. *et al.* GLUT1 deficiency and other glucose transporter diseases. *Eur. J. Endocrinol.* **150**, 627–633 (2004).
- Scheepers, A., Joost, H. G. & Schurmann, A. The glucose transporter families SGLT and GLUT: molecular basis of normal and aberrant function. *JPEN J. Parenter. Enteral Nutr.* **28**, 364–371 (2004).
- Faham, S. *et al.* The crystal structure of a sodium galactose transporter reveals mechanistic insights into Na<sup>+</sup>/sugar symport. *Science* **321**, 810–814 (2008).
- Mueckler, M. Facilitative glucose transporters. *Eur. J. Biochem.* **219**, 713–725 (1994).
- Mueckler, M. *et al.* Sequence and structure of a human glucose transporter. *Science* **229**, 941–945 (1985).
- Klepper, J. Glucose transporter deficiency syndrome (GLUT1DS) and the ketogenic diet. *Epilepsia* **49** (Suppl 8), 46–49 (2008).
- Brockmann, K. The expanding phenotype of GLUT1-deficiency syndrome. *Brain Dev.* **31**, 545–552 (2009).
- Scheffer, I. E. GLUT1 deficiency: a glut of epilepsy phenotypes. *Neurology* **78**, 524–525 (2012).
- Santer, R. *et al.* Mutations in GLUT2, the gene for the liver-type glucose transporter, in patients with Fanconi-Bickel syndrome. *Nature Genet.* **17**, 324–326 (1997).
- Leturque, A., Brot-Laroche, E. & Le Gall, M. GLUT2 mutations, translocation, and receptor function in diet sugar managing. *Am. J. Physiol. Endocrinol. Metab.* **296**, E985–E992 (2009).
- Simpson, I. A. *et al.* The facilitative glucose transporter GLUT3: 20 years of distinction. *Am. J. Physiol. Endocrinol. Metab.* **295**, E242–E253 (2008).
- Amann, T. & Hellerbrand, C. GLUT1 as a therapeutic target in hepatocellular carcinoma. *Expert Opin. Ther. Targets* **13**, 1411–1427 (2009).
- Macheda, M. L., Rogers, S. & Best, J. D. Molecular and cellular regulation of glucose transporter (GLUT) proteins in cancer. *J. Cell. Physiol.* **202**, 654–662 (2005).
- Mueckler, M. The molecular biology of glucose transport: relevance to insulin resistance and non-insulin-dependent diabetes mellitus. *J. Diabetes Complications* **7**, 130–141 (1993).
- Leney, S. E. & Tavaré, J. M. The molecular basis of insulin-stimulated glucose uptake: signalling, trafficking and potential drug targets. *J. Endocrinol.* **203**, 1–18 (2009).
- Nelson, D. L. & Cox, M. M. *Lehninger Principles of Biochemistry* 1158 (W. H. Freeman, 2008).
- Pao, S. S., Paulsen, I. T. & Saier, M. H. Jr. Major facilitator superfamily. *Microbiol. Mol. Biol. Rev.* **62**, 1–34 (1998).
- Henderson, P. J. & Maiden, M. C. Homologous sugar transport proteins in *Escherichia coli* and their relatives in both prokaryotes and eukaryotes. *Phil. Trans. R. Soc. Lond. B* **326**, 391–410 (1990).
- Ozcan, S. & Johnston, M. Function and regulation of yeast hexose transporters. *Microbiol. Mol. Biol. Rev.* **63**, 554–569 (1999).
- Buttner, M. The monosaccharide transporter(-like) gene family in *Arabidopsis*. *FEBS Lett.* **581**, 2318–2324 (2007).
- Li, F. *et al.* Characterization of sucrose transporter alleles and their association with seed yield-related traits in *Brassica napus* L. *BMC Plant Biol.* **11**, 168 (2011).
- Mueckler, M. & Makepeace, C. Model of the exofacial substrate-binding site and helical folding of the human Glut1 glucose transporter based on scanning mutagenesis. *Biochemistry* **48**, 5934–5942 (2009).
- Abramson, J. *et al.* Structure and mechanism of the lactose permease of *Escherichia coli*. *Science* **301**, 610–615 (2003).
- Huang, Y., Lemieux, M. J., Song, J., Auer, M. & Wang, D. N. Structure and mechanism of the glycerol-3-phosphate transporter from *Escherichia coli*. *Science* **301**, 616–620 (2003).
- Yin, Y., He, X., Szewczyk, P., Nguyen, T. & Chang, G. Structure of the multidrug transporter EmrD from *Escherichia coli*. *Science* **312**, 741–744 (2006).
- Dang, S. *et al.* Structure of a fucose transporter in an outward-open conformation. *Nature* **467**, 734–738 (2010).
- Newstead, S. *et al.* Crystal structure of a prokaryotic homologue of the mammalian oligopeptide-proton symporters, PepT1 and PepT2. *EMBO J.* **30**, 417–426 (2011).
- Lam, V. M., Daruwalla, K. R., Henderson, P. J. & Jones-Mortimer, M. C. Proton-linked D-xylose transport in *Escherichia coli*. *J. Bacteriol.* **143**, 396–402 (1980).
- Davis, E. O., Jones-Mortimer, M. C. & Henderson, P. J. Location of a structural gene for xylose-H<sup>+</sup> symport at 91 min on the linkage map of *Escherichia coli* K12. *J. Biol. Chem.* **259**, 1520–1525 (1984).
- Davis, E. O. & Henderson, P. J. The cloning and DNA sequence of the gene xylE for xylose-proton symport in *Escherichia coli* K12. *J. Biol. Chem.* **262**, 13928–13932 (1987).
- Maiden, M. C., Davis, E. O., Baldwin, S. A., Moore, D. C. & Henderson, P. J. Mammalian and bacterial sugar transport proteins are homologous. *Nature* **325**, 641–643 (1987).
- Henderson, P. J. Proton-linked sugar transport systems in bacteria. *J. Bioenerg. Biomembr.* **22**, 525–569 (1990).
- Scrapanti, E. & Hunte, C. Discontinuous membrane helices in transport proteins and their correlation with function. *J. Struct. Biol.* **159**, 261–267 (2007).
- Snider, C. & White, S. *Membrane Proteins of Known 3D Structure* (Stephen H. White Lab., Univ. of California Irvine, 2011).
- Lu, F. *et al.* Structure and mechanism of the uracil transporter UraA. *Nature* **472**, 243–246 (2011).
- Ressi, S., Terwisscha van Scheltinga, A. C., Vonnrhein, C., Ott, V. & Ziegler, C. Molecular basis of transport and regulation in the Na<sup>+</sup>/betaine symporter BetP. *Nature* **458**, 47–52 (2009).
- Gao, X. *et al.* Structure and mechanism of an amino acid antiporter. *Science* **324**, 1565–1568 (2009).
- Fang, Y. *et al.* Structure of a prokaryotic virtual proton pump at 3.2 Å resolution. *Nature* **460**, 1040–1043 (2009).
- Gao, X. *et al.* Mechanism of substrate recognition and transport by an amino acid antiporter. *Nature* **463**, 828–832 (2010).
- Desai, T. A. & Rao, C. V. Regulation of arabinose and xylose metabolism in *Escherichia coli*. *Appl. Environ. Microbiol.* **76**, 1524–1532 (2010).
- Xiang, Z., Steinbach, P. J., Jacobson, M. P., Friesner, R. A. & Honig, B. Prediction of side-chain conformations on protein surfaces. *Proteins* **66**, 814–823 (2007).
- Wang, D. *et al.* Glut-1 deficiency syndrome: clinical, genetic, and therapeutic aspects. *Ann. Neurol.* **57**, 111–118 (2005).
- Cunningham, P., Afzal-Ahmed, I. & Naftalin, R. J. Docking studies show that D-glucose and quercetin slide through the transporter GLUT1. *J. Biol. Chem.* **281**, 5797–5803 (2006).
- Brockmann, K. *et al.* Autosomal dominant Glut-1 deficiency syndrome and familial epilepsy. *Ann. Neurol.* **50**, 476–485 (2001).
- Ho, Y. Y. *et al.* Glucose transporter type 1 deficiency syndrome (Glut1DS): methylxanthines potentiate GLUT1 haploinsufficiency *in vitro*. *Pediatr. Res.* **50**, 254–260 (2001).
- Franco, P. J. & Brooker, R. J. Functional roles of Glu-269 and Glu-325 within the lactose permease of *Escherichia coli*. *J. Biol. Chem.* **269**, 7379–7386 (1994).
- Guan, L. & Kaback, H. R. Lessons from lactose permease. *Annu. Rev. Biophys. Biomol. Struct.* **35**, 67–91 (2006).
- Schneider, T. R. & Sheldrick, G. M. Substructure solution with SHELXD. *Acta Crystallogr. D* **58**, 1772–1779 (2002).
- DeLano, W. L. The PyMOL Molecular Graphics System. <http://www.pymol.org> (2002).

**Supplementary Information** is available in the online version of the paper.

**Acknowledgements** We thank J. He, L. Tang, F. Yu and S. Huang at Shanghai Synchrotron Radiation Facility, and K. Hasegawa and T. Kumasaka at the SPring-8 beamline BL41XU, for on-site assistance. This work was supported by funds from the Ministry of Science and Technology (grant numbers 2009CB918802 and 2011CB910501), projects 31125009 and 91017011 of the National Natural Science Foundation of China, and funds from Tsinghua University.

**Author Contributions** L.S., X.Z. and N.Y. designed all experiments. L.S., X.Z., C.Y., X.G. and N.Y. performed the experiments for structural determination, homology-based structure modelling and biochemical analysis. X.S. and Y.R. synthesized 6-BrGlc. All authors analysed the data and contributed to manuscript preparation. N.Y. wrote the manuscript.

**Author Information** The atomic coordinates and structure factors of XylE bound to D-xylose, D-glucose and 6-BrGlc are deposited in the Protein Data Bank with accession codes 4GBY, 4GBZ and 4GC0. Reprints and permissions information is available at [www.nature.com/reprints](http://www.nature.com/reprints). The authors declare no competing financial interests. Readers are welcome to comment on the online version of the paper. Correspondence and requests for materials should be addressed to N.Y. ([nyan@tsinghua.edu.cn](mailto:nyan@tsinghua.edu.cn)).

## METHODS

**Preparation of the phylogenetic tree.** Sequences of 84 members in the SP family 2.A.1.1, excluding six redundant sequences for the same proteins, in the Transporter Classification Database (TCDB)<sup>51,52</sup> were aligned by using ClustalW<sup>53</sup>. The sequence alignment result was presented as phylogenetic tree by using the program PHYLIP<sup>54</sup>.

**Protein preparation.** The cDNA of full-length XylE from *E. coli* strain O157:H7 was subcloned into pET15b (Novagen). Overexpression of XylE was induced in *E. coli* BL21(DE3) by 0.2 mM isopropyl  $\beta$ -D-thiogalactoside (IPTG) when the cell density reached a  $D_{600}$  of 1.5. The *E. coli* cells were grown in 2-l flasks with 1 l of Luria–Bertani medium. For each batch of protein purification, 12 flasks were incubated in shakers (New Brunswick Scientific) at 300 r.p.m. After growth for 4 h at 37 °C, the cells were harvested, homogenized in buffer containing 25 mM Tris-HCl pH 8.0 and 150 mM NaCl, and disrupted with a French press with two passes at 10,000–15,000 lb in<sup>-2</sup>. Cell debris was removed by low-speed centrifugation for 10 min. The supernatant was collected and ultracentrifuged at 150,000g for 1 h. The membrane fraction was harvested and incubated for 1 h with 1.5% (w/v) dodecyl- $\beta$ -D-maltopyranoside (DDM; Anatrace) at 4 °C. After another ultracentrifugation step at 150,000g for 30 min, the supernatant was collected and loaded onto Ni<sup>2+</sup>-nitrilotriacetate affinity resin (Ni-NTA; Qiagen) and rinsed with buffer containing 25 mM Tris-HCl pH 8.0, 150 mM NaCl, 20 mM imidazole and 0.02% DDM. The protein was eluted from the affinity resin with buffer containing 25 mM Tris-HCl pH 8.0, 150 mM NaCl, 250 mM imidazole and 0.02% DDM. After removal of the hexahistidine tag, the protein was concentrated to about 10 mg ml<sup>-1</sup> before further purification by gel filtration (Superdex-200; GE Healthcare) in buffer containing 25 mM Tris-HCl pH 8.0, 150 mM NaCl and various detergents, with or without the targeted ligands. The peak fractions were collected and flash-frozen in liquid nitrogen.

All the XylE mutants were generated with a standard PCR-based strategy and were subcloned, overexpressed and purified in the same way as the wild-type protein.

**Synthesis of 6-BrGlc.** D-Glucose (20.0 g, 0.111 mol) was placed in a 1,000-ml round-bottomed flask, and pyridine (300 ml) was added. Some glucose remained undissolved. *p*-Toluensulphonyl chloride (22.0 g, 0.115 mol) was added at room temperature (27 °C). After stirring for 11 h, acetic anhydride (80 ml, 0.83 mol) was added in one portion. A gentle exothermic reaction took place. After being stirred for 1.5 h, the mixture was evaporated. Ethanol (200 ml) was added to a residual oil. The oil was dissolved and soon a white crystal appeared. After the mixture had stood undissolved at -10 °C for 27 h, the crystal was collected on a glass filter, washed with cold ethanol (25 ml, twice), and dried under reduced pressure. 6-*O*-(*p*-Toluensulphonyl)-1,2,3,4-tetra-*O*-acetyl- $\beta$ -D-glucose (compound 1) was obtained in 33% yield (18.5 g, 36.8 mmol). Compound 1 (1.2 g, 4.0 mmol) was placed in a 100-ml round-bottomed flask. Acetone (5 ml) and tetra-*n*-butylammonium bromide (9.0 g, 28.0 mmol) were added. The resulting mixture was heated under reflux for 20 h. The reaction proceeded gradually. The mixture was poured into 100 ml of water, and the resulting solid was filtered with a glass filter. Recrystallization from ethanol afforded 6-bromo-6-deoxy-1,2,3,4-tetra-*O*-acetyl- $\beta$ -D-glucose (compound 2) in 50% yield (0.82 g, 2.0 mmol). Compound 2 (2,300 mg, 0.73 mmol) was placed in a 50-ml round-bottomed flask. Sulphuric acid (0.5 M aqueous solution, 12 ml) and acetonitrile (2.4 ml) were added to the flask, and the mixture was heated at 80 °C for 4 h. After cooling to room temperature, sodium hydrogen carbonate was carefully added in portions to the acidic solution. Neutralization was checked with indicator paper, and the mixture was then directly evaporated (bath temperature 40 °C). Before complete removal of solvent (about 10–20 ml), methanol (10 ml) was added to the flask, which led to the growth of a white precipitate. Filtration through Celite, concentration of the filtrate, and silica gel column purification (dichloromethane:methanol = 10:1) yielded 6-bromo-6-deoxy-D-glucose (124 mg, 0.51 mmol; 70%). The structure of the final product was confirmed by both NMR and high-resolution mass spectrometric analysis.

**Crystallization.** Extensive crystallization trials were performed for XylE proteins purified in various detergents. Crystals were grown at 18 °C by the hanging-drop vapour diffusion method. Several crystal forms of ligand-free XylE were obtained; however, none of these crystals diffracted X-rays beyond 10 Å at synchrotron beamlines. We reasoned that substrate–inhibitor binding might help to stabilize protein conformation, thus improving crystal packing<sup>36</sup>. The full-length wild-type XylE protein (with a final concentration of about 0.1 mM) purified in 0.2% *n*-nonyl- $\beta$ -D-glucopyranoside (Anatrace), 0.02% *n*-dodecyl-*N,N*-dimethylamine-*N*-oxide and 20 mM D-xylose gave rise to crystals in multiple poly(ethylene glycol) (PEG) conditions. The crystals tested on a home X-ray source diffracted to about 8–10 Å. After optimization, XylE crystals appeared overnight in the well buffer containing 40% (w/v) PEG400, 0.05 M glycine pH 9.6, 0.1 M LiCl, and diffracted to about 2.8 Å at Spring-8 beamline BL41XU. Heavy-atom derivative crystals were obtained by soaking crystals for about 1 h in mother liquor containing 1 mg ml<sup>-1</sup> K<sub>2</sub>PtCl<sub>4</sub> or CH<sub>3</sub>HgCl. Both native and heavy-atom-derived crystals were directly flash-frozen

in a cold nitrogen stream at 100 K. Crystals were also obtained under similar conditions with 40 mM D-glucose or 6-Br-Glc replacing D-xylose, and the best diffractions were obtained at about 2.9 and 2.6 Å, respectively.

**Data collection and structural determination.** All data sets were collected at Shanghai Synchrotron Radiation Facility beamline BL17U or SPring8 beamline BL41XU and processed with the HKL2000 package<sup>55</sup>. Further processing was performed with programs from the CCP4 suite<sup>56</sup>. Data collection and structure refinement statistics are summarized in Supplementary Table 1.

The initial phases of D-xylose-bound XylE were obtained from the Hg-derivative crystals by single anomalous diffraction (SAD) using the program ShelxC/D/E<sup>49</sup>. The electron density shows that there is one molecule in each asymmetry unit. Then a crude helical model was built manually using the program COOT<sup>57</sup>. With this partial model as input, the identified Hg atom positions were refined and phases were recalculated using the PHASER SAD experimental phasing module<sup>58</sup>. Since the *c* dimension of the unit cell in a Pt-SAD data set (*c* = 175.2 Å) is significantly different from that in the Hg-SAD data (*c* = 166.6 Å) and the native data (*c* = 168.2 Å), cross-crystal averaging combined with solvent flattening and histogram matching was performed using all three data sets by DMMulti<sup>59</sup>, which gave rise to a significantly improved electron density map. With the improved map, the crude model was rebuilt using COOT and refined with PHENIX<sup>60</sup>.

The structures of XylE bound to D-glucose and 6-BrGlc were solved by molecular replacement, with the D-xylose-bound XylE structure as the search model using the program PHASER<sup>58</sup>. The structure was manually refined with PHENIX and COOT iteratively.

**Preparation of liposomes and proteoliposomes.** Liposomes were prepared using a standard protocol as described previously<sup>61</sup>. Proteoliposomes for the D-[1-<sup>3</sup>H]xylose and D-[1-<sup>3</sup>H(N)]glucose (American Radiolabeled Chemicals, Inc.) counterflow assay were prepared in a solution containing KPM 6.5 buffer (50 mM potassium phosphate, 2 mM MgSO<sub>4</sub> pH 6.5), 20 mg ml<sup>-1</sup> pre-extruded phospholipids (*E. coli* polar lipids; Avanti), 1% *n*-octyl- $\beta$ -D-glucoside ( $\beta$ -OG; Anatrace), 20 mM D-xylose or D-glucose, and WT or mutant XylE proteins at a concentration of 10  $\mu$ g protein per mg lipid.  $\beta$ -OG was removed by incubation overnight with 400 mg ml<sup>-1</sup> Bio-Beads SM2 (Bio-Rad). After the removal of  $\beta$ -OG, the proteoliposomes were frozen and thawed for five cycles. After extrusion through a 400-nm membrane filter, the proteoliposomes were harvested by ultracentrifugation at 100,000g for 1 h and washed twice with ice-cold KPM 6.5 buffer to remove the extra sugar. The proteoliposomes were resuspended in ice-cold KPM 6.5 buffer to a final concentration of 100 mg ml<sup>-1</sup> immediately before the counterflow assay.

**Counterflow assay.** All counterflow assays were performed at 25 °C. For each assay, 2  $\mu$ l of concentrated proteoliposomes preloaded with 20 mM substrates were diluted into 100  $\mu$ l of assay buffer containing 1  $\mu$ Ci of D-[<sup>3</sup>H]xylose (specific radioactivity 12 Ci mmol<sup>-1</sup>) or D-[<sup>3</sup>H]glucose (specific radioactivity 20 Ci mmol<sup>-1</sup>). The final concentration of the external D-[<sup>3</sup>H]xylose was 0.83  $\mu$ M. For the sugar competition assay, indicated pentoses or hexoses were included at 10 mM in the external solution. The uptake of radiolabelled substrates was allowed for 30 s, if not otherwise indicated, by rapidly filtering the solution through 0.22- $\mu$ m filters (Millipore). After filtration, the filter membranes were washed with 2 ml of ice-cold reaction buffer without sugar. The filter was then taken for liquid scintillation counting. The time-course experiments showed that the accumulation of D-xylose was roughly linear within the first 30 s. Therefore, to determine the  $K_m$  and  $V_{max}$  of D-xylose uptake by WT XylE, the initial velocities were measured at 15 s. The sugar concentration in the assay buffer was adjusted by non-radiolabelled substrate. The data were fitted to the Michaelis–Menten equation,  $V = (V_{max}[D\text{-xylose}]) / (K_m + [D\text{-xylose}])$ , in GraphPad Prism 5.0 Demo. All experiments were repeated at least three times. Error bars represent s.d.

**Counterflow assay under variable pH values.** XylE-free liposomes or XylE inserted proteoliposomes were preloaded with 20 mM cold D-xylose in KPM buffer (50 mM potassium phosphate, 2 mM MgSO<sub>4</sub>, pH adjusted as indicated). At time point zero, concentrated proteoliposomes (2  $\mu$ l) were diluted into 100  $\mu$ l of KPM buffer (at the same pH as the proteoliposomes were prepared in) containing 1  $\mu$ Ci of D-[<sup>3</sup>H]xylose. The reaction was stopped at the indicated time points by rapidly filtering the solution through 0.22- $\mu$ m filter membranes (Millipore) and washed with 2 ml of ice-cold buffer. The filter was then taken for liquid scintillation counting. All experiments were repeated at least three times. Error bars represent s.d.

**Cell-based uptake assay.** The *xylE*-deficient *E. coli* strain Keio Collection JW3991 used in this assay was purchased from the National BioResource Project (NIG, Japan). Wild-type (WT) and XylE variants containing indicated missense point mutations were subcloned into pQLINK vector<sup>62</sup> with a His<sub>6</sub> tag at the C terminus. The membrane expression level of XylE variants was monitored by western blots with an antibody against the histidine tag. The amount of XylE proteins in the membrane fraction was estimated by comparing the intensity of

the proteins in the membrane fraction against a serial dilution of purified XylE with known concentrations on the same western blot, a protocol reported previously<sup>27</sup>.

The cell-based uptake assay was performed with the following protocol. *XylE*-deficient *E. coli* cells transformed with plasmids were grown in Luria–Bertani medium at 37 °C and induced with 50 µM IPTG for 30 min, when the cell density reached a  $D_{600}$  of about 1.5. Cells were then harvested by centrifugation. After being washed twice with MK buffer (150 mM KCl, 5 mM MES pH 6.5), the cells were resuspended in the same buffer to a  $D_{600}$  of 2.0. Before reaction, cells were energized by the addition of glycerol to a final concentration of 20 mM. To compare the transport activity of the XylE variants, D-<sup>3</sup>H]xylose was applied at 0.14 µM and each reaction was allowed for 30 s. Cells were taken at the indicated time for filtration through 0.45-µm cellulose acetate filter (Sartorius). The filter membranes were immediately washed with 2 ml of ice-cold MK buffer, dried, and taken for liquid scintillation counting. Control experiments were performed with cells transformed with an empty vector of pQLINK. All experiments were repeated at least three times. Error bars represent s.d. All the reactions were performed at 25 °C. All the XylE variants were expressed and quantified by following the same protocol as for WT XylE. The solution behaviour of the purified XylE variants was examined by size-exclusion chromatography, which showed similar profiles to that of WT protein.

Counterflow and cell-based uptake assays were also performed for the XylE variants shown in Figs 2c and 5c with an external D-<sup>3</sup>H]xylose concentration at 0.4 mM. The results remained almost identical to those seen in Figs 2c and 5c.

**Isothermal titration calorimetry.** The binding affinities between ligands and XylE variants were measured with an ITC200 microcalorimeter (MicroCal). Full-length WT or mutant XylE was extracted and purified through Ni-NTA resin in buffer containing 0.02% DDM. The eluate from Ni-NTA was concentrated and directly subjected to size-exclusion chromatography (Superdex-200; GE Healthcare) in buffer containing 0.015% DDM, 25 mM MES pH 6.5 and 150 mM NaCl. The peak fractions were pooled and concentrated to about 0.1 mM for isothermal titration calorimetry titration. The protein was titrated by 10 mM ligands dissolved in an identical buffer to that used for size-exclusion

chromatography at 22 °C. The data were fitted using the software Origin 7.0 (MicroCal).

**Homology modelling of human GLUT1.** Sequences of XylE from *E. coli* strain O157:H7 and human GLUT1–4 were first aligned with ClustalW (Fig. 1c)<sup>53</sup>. Using the alignment results and the crystal structure of XylE as input, we built the homology models of human GLUT1–4 with the software JACKAL<sup>42</sup>.

51. Saier, M. H. Jr, Yen, M. R., Noto, K., Tamang, D. G. & Elkan, C. The Transporter Classification Database: recent advances. *Nucleic Acids Res.* **37**, D274–D278 (2009).
52. Saier, M. H. Jr, Tran, C. V. & Barabote, R. D. TCDB: the Transporter Classification Database for membrane transport protein analyses and information. *Nucleic Acids Res.* **34**, D181–D186 (2006).
53. Thompson, J. D., Higgins, D. G. & Gibson, T. J. CLUSTAL W: improving the sensitivity of progressive multiple sequence alignment through sequence weighting, position-specific gap penalties and weight matrix choice. *Nucleic Acids Res.* **22**, 4673–4680 (1994).
54. Felsenstein, J. PHYLIP—Phylogeny Inference Package (version 3.2). *Cladistics* **5**, 164–166 (1989).
55. Otwinowski, Z. & Minor, W. Processing of X-ray diffraction data collected in oscillation mode. *Methods Enzymol.* **276**, 307–326 (1997).
56. Collaborative Computational Project Number 4. The CCP4 suite: programs for protein crystallography. *Acta Crystallogr. D* **50**, 760–763 (1994).
57. Emsley, P. & Cowtan, K. Coot: model-building tools for molecular graphics. *Acta Crystallogr. D* **60**, 2126–2132 (2004).
58. McCoy, A. J. *et al.* Phaser crystallographic software. *J. Appl. Cryst.* **40**, 658–674 (2007).
59. Cowtan, K. dm: an automated procedure for phase improvement by density modification. *Joint CCP4 ESF-EACBM Newsl. Prot. Crystallogr.* **31**, 34–38 (1994).
60. Adams, P. D. *et al.* PHENIX: building new software for automated crystallographic structure determination. *Acta Crystallogr. D* **58**, 1948–1954 (2002).
61. Veenhoff, L. M. & Poolman, B. Substrate recognition at the cytoplasmic and extracellular binding site of the lactose transport protein of *Streptococcus thermophilus*. *J. Biol. Chem.* **274**, 33244–33250 (1999).
62. Scheich, C., Kummel, D., Soumailakakis, D., Heinemann, U. & Bussow, K. Vectors for co-expression of an unrestricted number of proteins. *Nucleic Acids Res.* **35**, e43 (2007).